NMR and MD Simulations Reveal the Impact of the V23D Mutation on the Function of Yeast Oligosaccharyltransferase Subunit Ost4

Bharat P Chaudhary, David L Zoetewey[#], Martin J McCullagh, and Smita Mohanty*

Department of Chemistry, Oklahoma State University, Stillwater, OK, USA, 74078

Current Address: Department of Chemistry, Physics and Astronomy, Georgia College and State University, Milledgeville, GA, USA, 31061

*Corresponding author: Prof. Smita Mohanty, Department of Chemistry, Oklahoma State University, Stillwater, OK, USA, 74078, Email: smita.mohanty@okstate.edu

Keywords: Congenital disorders of glycosylation/Membrane protein/Molecular dynamics simulations/NMR/Oligosaccharyltransferase (OST)

Abstract

Asparagine-linked glycosylation, also known as *N*-linked glycosylation, is an essential and highly conserved co- and post-translational protein modification in eukaryotes and some prokaryotes. In the central step of this reaction, a carbohydrate moiety is transferred from a lipid-linked donor to the side-chain of a consensus asparagine in a nascent protein as it is synthesized at the ribosome. Complete loss of oligosaccharyltransferase (OST) function is lethal in eukaryotes. This reaction is carried out by a membrane-associated multi-subunit enzyme, OST, localized in the endoplasmic reticulum (ER). The smallest subunit, Ost4, contains a single membrane-spanning helix that is critical for maintaining stability and activity of OST. Mutation of any residue from Met^{18} to Ile^{24} of Ost4 destabilizes the enzyme complex, affecting its activity. Here, we report solution NMR structures and molecular dynamics simulations of Ost4 and Ost4V23D in micelles. Our studies revealed that while the point mutation did not impact the structure of the protein, it affected its position and solvent exposure in the membrane mimetic environment. Furthermore, our molecular dynamics simulations of the membrane-bound OST complex containing either WT or V23D mutant demonstrated disruption of most hydrophobic helix-helix interactions between Ost4V23D and transmembrane (TM)12 and TM13 of Stt3. This disengagement of Ost4V23D from the OST complex led to solvent exposure of the D23 residue in the hydrophobic pocket created by these interactions. Our study not only solves the structures of yeast Ost4 subunit and its mutant but also provides a basis for the destabilization of the OST complex and reduced OST activity.

Introduction

N-linked glycosylation is an essential and highly conserved co- and post-translational protein modification that occurs in some prokaryotes (Szymanski & Wren 2005, Wacker et al 2002) and nearly all eukaryotes (Cherepanova et al 2016, Dempski & Imperiali 2002, Larkin & Imperiali 2011). In eukaryotes, a preassembled mannose-rich tetradecaoligosaccharide ($Glc_3Man_9GlcNAc_2$) is transferred from the lipid-linked donor, dolichol pyrophosphate (DolPP), to an asparagine residue specified by a consensus sequence NXS/T (X proline) on the nascent polypeptide (Breitling & Aebi 2013, Chavan & Lennarz 2006, Helenius & Aebi 2004, Kornfeld & Kornfeld 1985). *N*-linked glycosylation occurs in the lumen of the endoplasmic reticulum (ER) as the nascent polypeptide chain emerges from the ribosome and is translocated *via* translocon. Oligosaccharyltransferase (OST), a membrane-associated multimeric enzyme complex in eukaryotes, carries out this protein modification. Following *N*-linked glycosylation, the correctly glycosylated proteins are folded properly and routed to their destinations. *N*-glycans are essential for protein folding, stability, activity, subcellular localization and intracellular trafficking, and many other critical processes (Gahmberg & Tolvanen 1996, Grigorian et al 2012, Helenius & Aebi 2004, Mohorko et al 2011). Genetic defects in the *N*-linked glycosylation pathway in humans cause a group of inherited rare metabolic disorders collectively known as congenital disorders of glycosylation (CDG) (Freeze 2013, Hennet & Cabalzar 2015).

OST is a remarkably complex multi-subunit enzyme for eukaryotes. For many higher eukaryotes, protein *N*-linked glycosylation is a highly coordinated and complex process. In contrast, a single subunit defines the OST activity in prokaryotes (ssOST),

emphasizing the complexity of the glycosylation process in eukaryotes. In the most extensively studied eukaryotic system, *Saccharomyces cerevisiae*, OST has two isoforms (Wild et al 2018). Seven membrane protein subunits (Ost1, Ost2, Ost4, Ost5, Stt3, Wbp1 and Swp1) are common to both isoforms while the eighth subunit (Ost3/Ost6) is an interchangeable homologue (Kelleher & Gilmore 2006, Mohanty et al 2020, Yan & Lennarz 2005). Five subunits (Ost1, Ost2, Stt3, Swp1 and Wbp1) are essential for cell growth, whereas the remaining three subunits (Ost4, Ost3/Ost6 and Ost5) are crucial for maintaining complex stability and optimal OST activity (Kelleher & Gilmore 2006, Mueller et al 2015). In the ER membrane, these subunits form three subcomplexes: subcomplex I (Ost1-Ost5), subcomplex II (Wbp1-Swp1-Ost2), and subcomplex III (Stt3-Ost4-Ost3/Ost6) (Karaoglu et al 1997). All of the yeast subunits have homologs in the mammalian OST complex (Cherepanova et al 2016, Mohanty et al 2020).

Despite the biological significance of *N*-linked glycosylation, the enzymatic mechanism and exact roles of each OST subunit have not been fully elucidated at the molecular level. A number of atomic resolution structures of either an individual subunit or a single domain have been determined. These include NMR structures of chemically synthesized Ost4 from yeast (Zubkov et al 2004) and humans (Gayen & Kang 2011) in a mixed organic solvent system, the crystal structure of the N-terminal luminal domain of Ost3/Ost6 (Schulz et al 2009), and the NMR structure of the yeast Stt3p catalytic subunit in micelles (Huang et al 2012). Additionally, the low-resolution cryo-EM structure of yeast OST has been previously reported (Li et al 2008). Comparison of the structures of eukaryotic OSTs with those from archaea (Matsumoto et al 2013) and bacteria (Lizak et al 2011) have

revealed that the overall mechanism of *N*-linked glycosylation is conserved across all domains of life (Mohanty et al 2020, Shrimal & Gilmore 2018). Recent advancement in high-resolution cryo-EM has enabled the atomic resolution structures of both yeast and human OST complexes (Bai et al 2018, Ramirez et al 2019, Wild et al 2018). However, there are many fundamental questions that still need to be addressed including the requirement of multiple subunits, the function of each subunit in *N*-linked glycosylation, and their roles in the stabilization of the multimeric enzyme complex. Discerning the role of each individual subunit through structure-function studies is critical for unraveling the necessity of multiple non-identical subunits in higher organisms.

The major limitation has been the difficulty in expression, purification, and reconstitution of integral membrane proteins (IMPs) in a suitable membrane-mimicking environment. Once a pure and homogeneous IMP is obtained, the next challenge is to determine a suitable membrane mimetic system for structure-function studies.

In yeast, OST4 encodes a single membrane-spanning protein containing 36 residues. This extraordinarily small membrane protein has been reported to bridge contacts between the Stt3 and Ost3 subunits in the Stt3-Ost4-Ost3/Ost6 subcomplex (Kim et al 2003). Furthermore, this mini-membrane protein is essential for the recruitment of Ost3 or Ost6 to the OST complex (Spirig et al 2005). In the recent cryo-EM structure of the yeast OST complex, the single transmembrane (TM) domain of Ost4 is nestled between two transmembrane helices (TMH1 and TMH13) of the catalytic subunit Stt3 (Bai et al 2018, Wild et al 2018). Mutation of any hydrophobic residue in position Met^{18} to Ile^{24} of

Ost4 to either a negative (aspartate) or positive (lysine) charged residue, results in a temperature-dependent growth phenotype and reduced *in vitro* OST activity (Kim et al 2000, Kim et al 2003). These mutations cause a 30% – 50% reduction in OST activity. Specifically, the Ost4V23D mutation reduces OST activity by 50% (Kim et al 2000). The mutation of M18K or V23D results in cell death at 37 ^{o}C (Kim et al 2000). However, mutation of M18L/G, V23L/G does not significantly affect cell growth or *in vitro* OST activity (Kim et al 2000). In contrast to the C-terminal TMH segment, no adverse effect on cell growth or OST activity was observed for a similar mutation of any residue in the N-terminal segment, Ile^{2} to Val^{17} of Ost4 (Kim et al 2000). We hypothesize that the C-terminal TMH segment, Met^{18} to Ile^{24} of Ost4 plays a pivotal role in the helix-helix interactions with the TMHs of Stt3. Mutation of even a single residue in this segment disrupts these interactions due to the change of either its structure or its position, resulting in the destabilization of the complex and the complete loss of OST activity. Comparative study of the structure and function of Ost4 and its functionally important mutant/s would provide insight into the role of these residues (Met^{18} to Ile^{24}), especially that of V23, in the stabilization of the enzyme.

Although atomic resolution structures are available for two eukaryotic Ost4s in 4:4:1 chloroform-methanol-water mixed organic solvent system, many questions regarding the impact of the mutation on the 3-dimensional structure and/or the orientation of the mutant protein/s in the membrane remain unanswered. Does this point mutation on TM helix of Ost4 disrupt its structure or its location in the membrane? In addition, questions such as “what would the structure be” if reconstituted in micelles are also equally important.

Although the above mixed-organic solvents system has been used as a membrane mimetic for the high-resolution structure determination of small IMPs using solution-state NMR (Dmitriev et al 1999, Girvin et al 1998, Rastogi & Girvin 1999, Szyperski et al 1998), such a solvent system is a marginal approximation of a non-polar membrane surrounded by an aqueous environment. Phospholipid micelles on the other hand are a considerably better mimetic of biological membranes. They contain a completely nonpolar core region of a similar thickness to a membrane that is surrounded by a layer of charges at the water interface similar to that of the lipid bilayer. DPC is a zwitterionic detergent that has a structure similar to phospholipid bilayers and has been extensively used in structural determination of membrane proteins by NMR (Kang & Li 2011, Lim et al 2017, Renault et al 2010).

We have previously reported overexpression, purification, and reconstitution of homogeneous recombinant Ost4 and its critical mutant Ost4V23D in dodecylphosphocholine (DPC) micelles (Chaudhary et al 2017, Kumar et al 2012). Here, we report the solution NMR structures and molecular dynamics (MD) simulations of Ost4 and Ost4V23D in DPC micelles performed under similar conditions. Our results provide insight into the impact of V23D mutation on Ost4 and its consequence on the local hydrophobicity of the Ost4V23 residue. We have shown that this mutation disturbs the interactions of Ost4 with the catalytic subunit Stt3, and increases the solvent exposure of this component of the complex.

Results

Chemical Shift Perturbation (CSP) in Ost4 due to V23D Mutation

By using far-UV circular dichroism (CD) and {^{1}H, ^{15}N}-HSQC spectroscopy, we have

previously reported that Ost4 and Ost4V23D in DPC micelles are well folded, and it is feasible to determine the 3D structures of these proteins in DPC micelles (Chaudhary et al 2017). The recombinant Ost4 and Ost4V23D proteins were expressed, purified and reconstituted in 100 mM deuterated DPC micelles for NMR data collection. Various heteronuclear 3D NMR experiments were used for complete resonance and NOE assignments of the Ost4 and Ost4V23D reconstituted in DPC micelles. We have recently reported the side-chain and backbone resonance assignments for the Ost4 and Ost4V23D proteins (Chaudhary et al 2020). The chemical shift perturbation (CSP) in Ost4 due to the V23D mutation was extensive (Fig. 1), requiring reassignment of the resonances in Ost4V23D independently by using various 3D NMR data sets. In Ost4V23D, the amide backbone resonance of L21, I22, D23, and A27 residues shifted dramatically (Fig. 1). The CSP was quantified as $0.5[™_H^2+(0.3™_N^2)]$, where $™_H$ and $™_N$ are observed chemical shift changes for ^{1}H and ^{15}N shifts in ppm, respectively. The CSPs for these residues were > 0.5 ppm (Fig. 1b).

Distance restraint analysis and structure calculation of Ost4 and Ost4V23D

The secondary structures of Ost4 and Ost4V23D (Fig. 2) clearly indicated that both proteins contain a single ⟨-helix encompassing residues Asp^4 to Met^{32} (Chaudhary et al 2020). Secondary structure elements such as alpha-helix and beta-sheet produce characteristic sequential and medium-range nuclear Overhauser effect (NOE) peaks that can help confirm their presence within a protein sequence. We observe the common alpha-helical NOE cross-peaks between residues consistently from amino acid Asp^4 to Met^{32} except one strong $d_{⟨N(i,\ i+1)}$ peak between residues Ile2 to Ser3 (Fig. 2). The

sequential NOE pattern (Fig. 2) suggests an alpha-helical secondary structure for the Asp^{4} to Met^{32} consistent with what we have reported previously based on chemical shifts values using $TALOS^{+}$ (Chaudhary et al 2020). The cross-peaks from 3D NOE spectra for each protein was converted into upper distance limits, which were finally used for the determination of 3D structures of both Ost4 and Ost4V23D, separately. A summary of NOE connectivity of Ost4 and Ost4V23D proteins, along with their secondary structural elements, is illustrated in Fig. 2.

For structure calculation, dihedral angles were derived from backbone chemical shift using the TALOS+ program incorporated in NMRPipe. All distance constraints used for structure calculation were derived from a combination of separate 3D NOESY experiments. Together, these NOE restraints enabled us to calculate the 3D structures of Ost4 and Ost4V23D. The ensemble structure of both Ost4 (Fig. 3a) and Ost4V23D (Fig. 3c) were independently calculated using different sets of NOE restraints. The backbone root mean square deviation (RMSD) value of the 20 lowest energy structures to the mean was 0.24 Å and 0.20 Å for Ost4 and Ost4V23D, respectively (Table I). The structures show that both proteins contain a well-defined ⟨-helix encompassing residues Asp^{4} to Met^{32} with N-terminal residues Met^{1} to Ser^{3} and the C-terminal residues Ser^{33} to Asn^{36} being random coil. Surprisingly, the 3D structures of both Ost4 (Fig. 3b) and its critical mutant Ost4V23D (Fig. 3d) were found to be nearly identical in DPC micelles with a backbone RMSD of 0.75 Å for all residues.

Comparison of Ost4 structure in Different Membrane Mimetic

The solution NMR structures of yeast and human Ost4 determined on chemically synthesized proteins in a mixed organic solvent system contained a kink in the transmembrane helix (TMH) (Fig. 4a) (Gayen & Kang 2011, Zubkov et al 2004). However, no kink is present in the NMR structure of Ost4 determined here in DPC micelles (Fig. 3). Indeed, the backbone RMSDs for the entire helical region (residues Asp^{4} to Met^{32}) between recombinant Ost4 structure in DPC micelles and those of the chemically synthesized yeast and human Ost4 structures in mixed organic solvents were 2.92 Å and 2.47 Å, respectively. In contrast, the Ost4 structures in the yeast and human OST complexes, determined by cryo-EM in nanodisc or digitonin, were shown to contain a single straight TMH (Bai et al 2018, Ramirez et al 2019, Wild et al 2018). Moreover, the current Ost4 NMR structure in DPC micelles fits very well to the yeast Ost4 structure determined in nanodisc or digitonin with backbone RMSDs of 0.68 Å and 1.04 Å, respectively (Fig. 4b). Likewise, the backbone RMSDs of the Ost4 structure in DPC micelles to human Ost4 from OST-A or OST-B complex were 0.46 Å and 0.76 Å, respectively (Fig. 4c).

Molecular Dynamics Simulation of Ost4 in DPC Micelles

MD simulations were performed on Ost4 and Ost4V23D in DPC micelles to get insight into their orientation in the membrane mimetic. Each MD simulation was carried out for 150 ns. Both systems reached a stable structural ensemble within the time scale of the simulation. The average backbone RMSDs of the proteins plateaued at ~0.6 nm with relatively small fluctuations after 40 ns for WT (Fig. 5a) while the mutant took 110 ns (Fig. 5b). Subsequent analyses were performed on the last 40 ns of simulation for both

systems.

MD simulations of both Ost4 and Ost4V23D revealed conflicting behavior in the membrane environment despite the fact that their NMR structures are nearly identical in DPC micelles. The WT Ost4 remained in the center of the DPC micelle (Fig. 6a and b). Residues Met^{1} to Ser^{9} and Asp^{29} to Asn^{36} are solvent-exposed while residues Leu^{10} to Val^{28} of the ⟨-helix reside inside the hydrophobic core of the DPC micelles (Fig. 6a and b). By contrast, Ost4V23D positioned itself at the interface between the micelle and the solvent (Fig. 6c and d). The solvent exposure of residues Leu^{10} to Val^{28} of both proteins was quantified using the Solvent Accessible Surface Area (SASA) fraction. This is defined as the ratio between the water exposed surface area and the total surface area of a given selection of the peptide. The SASA fraction of hydrophobic residues of Ost4 (0.0662 ± 0.0003) was found to be smaller than that of Ost4V23D (0.2023 ± 0.0007). Similarly, the hydrophilic SASA fraction was smaller for Ost4 (0.1718 ± 0.0009) compared to Ost4V23D (0.428 ± 0.001, Fig. 7a). Additionally, the number of interactions between DPC tails and residues 10-28 were calculated for both proteins. About 64 ± 12 contacts were found between Ost4 residues Leu^{10} to Val^{28} and the DPC tails, whereas only 16 ± 6 contacts were observed between the same region of Ost4V23D protein and the DPC tails (Fig. 7b).

Molecular Dynamics Simulation of Membrane-Bound OST Complex

MD Simulations of components of the OST complex, including the transmembrane (TM) helix of Ost1, Ost3, Ost4, Ost5, and the transmembrane helices of Stt3 (other than TM

helix 9), were performed to investigate the structural perturbations of the Ost4V23D mutation. The TM helices of Ost2, Wbp1, and Swp1 were excluded from the MD simulation as they were beyond 10 Å from Ost4. These simulations were initiated in the CryoEM structure 6ezn (Wild et al 2018) and embedded in a membrane of dipalmitoylphosphatidylcholine (DPPC) lipids. Over the course of 600 ns of simulation, both the WT and Ost4V23D mutant remained embedded in the membrane. The mutant demonstrated local structural perturbations compared to the WT. Specifically, numerous hydrophobic contacts between Ost4V23 (brown) with Stt3 TM12, residue F425 and TM13 (red), residues I456 and L459, and with lipid tails (cyan) were observed in our WT simulation (Fig. 8a). While only a single a contact between Ost4D23 and Stt3I456 was maintained in the mutant, the carboxylate functional group of the aspartate formed a new stable salt bridge with Stt3K448 (Fig. 8b). These representative snapshots demonstrate the local structural perturbations observed due to the Ost4V23D mutation. Table-II lists Average minimum distance between atoms of residue 23 of WT and mutant with partner residues from TM-12 and TM-13 of Stt3 from molecular dynamics trajectories.

The increased hydrophilic nature of the Ost4 helix in the Ost4V23D mutant also lead to additional solvent exposure of that residue in the mutant simulation. This is quantified by the solvent accessible surface area (SASA) of the Ost4V23 residue in the WT and the Ost4V23D residue in the mutant (Fig. 8c). The mutant simulation demonstrates an average SASA of 0.15 nm^2 for this residue while the WT simulation has an almost zero SASA for this residue. The increase in solvent exposure in the mutant is due to the

destabilization of the buried hydrophobic pocket depicted in Fig. 8a. Additionally, hydrophobic contacts between the mutated D23 and the lipid tails are no longer observed. This behavior indicates that water penetrates the mutant protein to a greater degree than the WT.

Discussion

N-linked glycosylation is an essential and highly conserved co-and post-translational protein modification in all domains of life. Systematic mutagenesis studies on Ost4 revealed an impact on cell growth and *N* - glycosylation activity of the OST complex only when a hydrophobic residue in the TM segment, Met^{18} to Ile^{24}, is mutated to a charged residue (Kim et al 2000). However, the similar mutation in the N-terminal TM segment of Ost4 has no such effect on cell growth or OST activity. Likewise, conservative mutation of any residues in the TM segment, Met^{18} to Ile^{24}, has no negative effect on cell growth or OST activity. Specifically, V23G mutation did not impact cell growth or OST activity while V23D or V23K mutations each negatively did impact the cell growth and OST activity (Kim et al 2000). Compared to WT Ost4, Ost4V23D and Ost4V23K mutations reduce OST activity by 50% and 65%, respectively (Kim et al 2000).

We undertook a detailed structure-function study of Ost4 and Ost4V23D to investigate the effect of a charged residue in the transmembrane helix that abolishes the OST activity with a temperature-sensitive phenotype. We have previously reported that the impact of this point mutation is dramatic, as demonstrated by circular dichroism (CD) and 2D {^{1}H, ^{15}N} HSQC NMR (Chaudhary et al 2017, Chaudhary et al 2020). The mutation caused a

significant chemical shift perturbation for nearly all residues in the 2D {^{1}H, ^{15}N} HSQC spectrum of the mutant protein (Fig. 1). This perturbation could be due to a structural change in the protein, or a change in its chemical environment, or both. However, both Ost4 and Ost4V23D displayed nearly identical NMR structures (Fig. 3), suggesting that the chemical environments around the proteins are possibly different.

Both Ost4 and Ost4V23D are composed of a single ⟨□helix encompassing residues 4-32 (Fig. 3). This structure in DPC micelles is quite similar to the single helix that was reported recently for Ost4 as part of the OST complex solved either in nanodisc or in detergent using cryo-EM (Fig. 4b) (Bai et al 2018, Wild et al 2018). The backbone (residues Asp^{4} to Met^{32}) RMSD between Ost4 solved here in DPC micelles and that of the Ost4 subunit in the OST complex solved in nanodisc is 0.68 Å (Fig. 4b). In contrast, the NMR structure of Ost4 determined in DPC micelles (Fig. 4a) was quite different than the NMR structure of Ost4 determined in mixed organic solvents (Gayen & Kang 2011, Zubkov et al 2004). The notable difference between these two NMR structures was the kink present in the NMR structure determined in mixed organic solvents (Gayen & Kang 2011, Zubkov et al 2004). In fact, the backbone RMSD between these structures was 2.92 Å. These results clearly demonstrate that DPC micelle is a closer mimic of a membrane bilayer than the mixed organic solvents system. Furthermore, the observed kink in the NMR structures determined in the mixed organic solvents system could be a structural artifact most likely attributable to the thickness of the non-polar to polar interface in this system. These observations are consistent with a previous report on the Step2 protein receptor fragment that exhibited different behavior and helical propensities in DPC micelles and

the mixed solvent system (Neumoin et al 2007). These authors likewise concluded that DPC micelles provide an environment that appears closer to that of a membrane bilayer than the mixed solvent system for observing the conformational preferences of small membrane proteins (Neumoin et al 2007). Moreover, the hydrophobic thickness of a micelle composed of 65 molecules of DPC in an MD simulation is 30 ±4 Å (Tieleman et al 2000) which fits well with an observed hydrophobic length of ~25 Å for Ost4 and is close to the hydrophobic width of 25-35 Å of a bilayer (Mashaghi et al 2012). It has been reported that lipid rearrangement can occur to completely cover the hydrophobic region of OmpX, a small membrane protein, in a similar micelle environment (Fernandez et al 2002).

The similarity of DPC micelle to the actual membrane thickness and its flexibility to adjust the width of the hydrophobic interior stands in contrast to a mixed organic solvents system that appears to have a narrower width and less flexibility in accommodating the transmembrane helix of Ost4. Therefore, we conclude that our structure of Ost4 in DPC micelles represents a realistic and reasonable reconstruction of its native environment.

MD simulations were performed for Ost4 and Ost4V23D separately in DPC micelles to determine the effect of the mutation on their behavior in a membrane-like environment. MD simulations have been frequently used to investigate the structural dynamics and orientation of membrane proteins in membrane environments (Hansson et al 2002, Hedger et al 2016, Kurauskas et al 2018, Wang & Tajkhorshid 2008). The chemical shift perturbation (Fig. 1) data suggested a change in the chemical environment of the wild type protein due to mutation since their structures were very similar under similar

conditions. By performing MD simulations, we were able to establish a likely explanation for the observed chemical shift perturbations throughout Ost4. Although both proteins were placed in a starting configuration in the center of the DPC micelle, simulation results showed that the wild type Ost4 maintained a very stable position in the center of the micelle (Fig. 6a and b). In fact, residues Leu^{10} to Val^{28} of Ost4 remained embedded in the micelles, indicating these residues are part of the transmembrane helix that spans the membrane. Based on the established orientation of Ost4, the N-terminal residues Met^{1} to Ser^{9} of Ost4 subunit remain in the ER lumen while the C-terminal residues Asp^{29} to Asn^{36} are exposed to the cytosol. The rest of the protein encompassing Leu^{10} to Val^{28} forms the transmembrane domain. This result is in agreement with the hydrophobicity profile as well as with the previously published report (Zubkov et al 2004). In the MD simulation of Ost4V23D in DPC micelles, the protein was placed in the center of the micelle. However, over the time course of the simulation, the position of the protein shifted towards the interface of DPC micelles and the solvent until it reached equilibrium (Fig. 6c and d). Thus, the mutant protein behaved like an amphipathic helix, partitioning between the micelles and aqueous phase by orienting its hydrophobic surface towards the interior of the micelle while exposing the hydrophilic face to the solvent (Fig. 6c and d, Fig. 7a). This result suggests that the single V23D mutation creates an amphipathic helix as opposed to the mainly hydrophobic helix of the WT. To understand the impact of this amphipathic helix in the OST complex, we carried out further MD simulations of both WT and Ost4V23D in the membrane-spanning portion of the OST complex.

Our studies indicated that the amphipathic helix did not dissociate from the Stt3

membrane-bound complex during 600 ns of MD simulation of the Ost4V23D mutant from a starting point of an intact complex. The mutation did, however, disrupt local hydrophobic contacts present in the WT complex (Fig. 8a and b). Table-II lists interactions between residue 23 of WT and mutant with partner residues from TM-12 and TM-13 of Stt3 with minimum distance shown. The V23D mutated residue formed a stable salt bridge with K448 of Stt3 TM13 as depicted in Fig. 8b. The formation of this salt bridge requires dislodging that residue from the hydrophobic pocket observed in the WT simulation that is composed of contacts made to F425 of TM12 as well as L459 and I456 of TM13 from Stt3 and two specific lipid molecules from the membrane as shown in Fig. 8a and Table-II. The hydrophilic aspartate residue becomes more solvent-exposed as the SASA of this residue increases from almost zero in the WT to 0.15 nm^2 in the Ost4V23D mutant (Fig. 8c). Taken together, these local disruptions are likely to cause significant disruption to the catalytic activity of Stt3.

The recent structure of the yeast OST complex shows that the Ost4 subunit is stacked in between several of the transmembrane helices of the catalytic subunit, Stt3 (Bai et al 2018). It was clear from MD simulations of the membrane-bound complex that the V23D mutation in Ost4 disrupts the hydrophobic interactions (Fig. 8a and Table-II) to these particular residues thereby disrupting the *N*-linked glycosylation process. The MD simulations also point to additional solvent exposure of the mutated residue suggesting additional disruption of the mutant complex due to the presence of water near this site.

Conclusion

A complete understanding of the structure, stabilization, and mechanism of function of each individual subunit as well as the whole yeast OST enzyme complex requires multiple approaches. Here, NMR spectroscopy identified the similarity in the 3D structures of the Ost4 and its critical mutant, Ost4V23D. However, MD simulations of the protein by itself or as part of the OST complex provided the most crucial information on the disengagement of the mutant from the catalytic subunit, Stt3. Specifically, the mutation disrupted almost all of the hydrophobic interactions between V23 to Stt3 and formed a new salt bridge between D23 to K448 causing distortion of TM13. This insight opens the door for further informative experimentation, and suggests an important role for TM13.

Methods

Protein Expression and Purification

GB1-Ost4 and GB1-Ost4V23D proteins were expressed and purified by following the procedure described previously (Chaudhary et al 2017, Kumar et al 2012). Briefly, the recombinant pET-3c/GB1-Ost4 and pET-3c/GB1-Ost4V23D plasmids were inserted into *Escherichia coli* BL21DE3pLysS cells. The expression was performed in M9 minimal media containing ^{15}N-labeled ammonium chloride and ^{13}C-labeled glucose. An overnight starter culture was diluted 1:25 (v/v) in minimal media and grown at 37 °C to an OD_{600} of 0.4-0.5. Expression was then induced with 1 mM IPTG at 30° C. After 8 h of incubation, the cells were harvested by centrifugation. The harvested cells were lysed by sonication using lysis buffer (50 mM phosphate buffer, pH 6.5, 200 mM NaCl, 0.01% sodium azide and 1 mM PMSF). After lysis, both proteins were purified by nickel-NTA affinity chromatography. The GB1 tag was cleaved with thrombin as described previously (Kumar et al 2012).^{15}N, ^{13}C-labeled Ost4/Ost4V23D proteins were purified and

reconstituted in DPC micelles (Chaudhary et al 2017).

NMR Data collection

All NMR data were acquired at 35 ^{o}C using either a Bruker Avance 800 MHz spectrometer with a triple resonance ^{1}H/^{13}C/^{15}N TCI cryoProbe equipped with z-axis pulsed field gradients at the National High Field Magnetic Laboratory, Tallahassee, Florida, Bruker Neo 700 MHz or 800 MHz spectrometers at Bruker BioSpin Corporation, Switzerland, or Varian Inova 600 MHz or 900 MHz spectrometers equipped with cold probes at the Department of Pharmacology, University of Colorado School of Medicine, Colorado. Some of the NMR data were collected on Bruker Avance 600MHz or Varian Inova 900 MHz spectrometers with cryoProbe at the University of Minnesota NMR center. All data were processed using NMRPipe (Delaglio et al 1995) and analyzed using NMRFAM-SPARKY (Lee et al 2015). For structure determination, samples between 300 µM and 1 mM of uniformly ^{15}N/^{13}C-labeled Ost4 or Ost4V23D in 50 mM phosphate buffer at pH 6.5 containing 1 mM EDTA, 0.01% NaN_3, 100 mM DPC and 5% D_2O were prepared. For complete backbone and side-chain assignments of Ost4 and Ost4V23D the following spectra were recorded at 35 ^{o}C: 2D {^{1}H,^{15}N}- HSQC (Kay et al 1992), 2D {^{1}H, ^{13}C}- HSQC, 3D HNHAHB, 3D HBHA(CO)NH, 3D HNCACB (Muhandiram & Kay 1994), 3D CBCA(CO)NH (Muhandiram & Kay 1994), 3D HNCA, 3D HN(CO)CA, 3D HCCH-TOCSY, 3D HCC(CO)NH-TOCSY (Grzesiek & Bax 1992), 3D and ^{15}N- edited HSQC-TOCSY (Norwood 1990) with an 85 ms mixing time. NOE distance restraints were collected from 3D ^{15}N-edited HSQC-NOESY (Norwood 1990, Zhang et al 1994) with mixing times of 90 ms and 120 ms.

Structure calculation and refinement

Structure calculations were performed using the CYANA 3.98beta program (Guntert & Buchner 2015). A total of 217 and 254 NOE cross-peaks for Ost4 and Ost4V23D proteins were assigned manually using NMRFAM-SPARKY, respectively (Lee et al 2015). The assignments were confirmed and/or corrected with the NOEASSIGN module of CYANA 3.98beta using the standard protocol of eight iterative cycles of NOE assignment and structure calculation (Guntert & Buchner 2015). During the iterative NOE assignments, 28 and 59 NOE peaks were removed because of ambiguity, overlap, or redundancy yielding a total of 189 and 195 NOE cross-peaks for Ost4 and Ost4V23D, respectively. The experimental upper distance limits were generated from the intensities of the assigned NOE cross-peaks using CYANA 3.98beta by using two calibration function: d^{-6} for backbone protons in residues 4-30 and d^{-4} for rest of the backbone and side-chain protons. A total of 68 dihedral angle restraints for Ost4 and 62 for Ost4V23D were derived from the assigned chemical shifts by using the program TALOS+ (Shen et al 2009). In addition, 27 hydrogen bond restraints (two restraints per bond) for Ost4 and Ost4V23D separately, were generated from the chemical shift index (CSI) by the program TALOS+. A total of 100 random structures were calculated using CYANA 3.98beta and 20 structures with the lowest target functions were selected for solvent refinement using CNS (Brunger et al 1998). The 20 structures having the lowest energy and the best Ramachandran statistics were assessed by PROCHECK (Laskowski et al 1996) and selected to represent the 3D structures of Ost4 and Ost4V23D in DPC micelles. The restraints used in NMR structures calculation of Ost4 and Ost4V23D and statistical parameters of the refined structures are provided in Table I. The structures were

visualized with Chimera (Pettersen et al 2004), VMD (Humphrey et al 1996), and Pymol (Schrodinger 2015). Figures were prepared with MOLMOL (Koradi et al 1996) or Chimera.

Molecular Dynamics

MD simulations of the micelle systems were performed using the GROMACS simulation package version 5.1.5 (Berendsen et al 1995). Initial protein micelles systems for Ost4 and Ost4V23D were derived from the membrane builder module of the CHARMM-GUI (Jo et al 2008, Lee et al 2016). The protein-micelles systems were built using 65 DPC detergent molecules. The systems were solvated with the TIP3P (Jorgensen et al 1983) water model and neutralized with Na^+ ions. All bonds containing hydrogen were constrained using the LINCS algorithm (Hess et al 1997) to enable a 2 fs time step. The temperature was kept constant at 308 K using Nose-Hoover coupling (Hoover 1985) with a 1ps coupling time constant. The pressure was maintained constant at 1bar using Parrinello-Rahman coupling (Nosé & Klein 1983, Parrinello & Rahman 1981) with a 5 ps coupling time constant. A cutoff of 1.2 nm was applied for van der Waals interactions. A cutoff of 1.2 nm for nonbonded interactions was used with a particle mesh Ewald (PME) treatment of the long-ranged electrostatics (Essmann et al 1995). The systems were subjected to <1000 steps of steepest descent energy minimization using the CHARMM36 force field (Huang & MacKerell 2013). For protein-micelles systems, 1 ns of NPT equilibration was performed after NVT equilibration. Finally, MD simulations of 150 ns for protein-micelles systems were carried out under similar conditions of NPT equilibration. Some of the computing for this project was performed at the OSU High-Performance

Computing Center at Oklahoma State University.

Membrane-bound systems of the WT and Ost4V23D system were created composed of Ost4, STT3, Ost1, Ost3, and Ost5 was simulated using the GPU accelerated Amber 18 software (Case et al). Ost2, Wbp1, and Swp1 were not included as they were beyond 10 Å from Ost4. The system was built from the initial cryoEM structure (Wild et al 2018) using the CHARMM GUI. The bilayer was composed of DPPC lipids with 307 in the upper leaflet and 320 in the lower leaflet. TIP3P water with a buffer size of 2.0 nm was added along with 0.1 M NaCl yielding a box of initial dimension 15x15x12.4 nm. The simulations were carried out in the NPT ensemble with anisotropic pressure coupling using the constant surface area. Combined, this system was 240K atoms and simulation of each system exceeded 600 ns.

The last 40 ns of the micelle simulations were used for analyses. Contact and root mean squared deviation (RMSD) analyses were performed using GROMACS inbuilt tools (distance and rms). Solvent accessible surface area (SASA) calculations were performed using the VMD tool. Here we compute the fraction of hydrophobic and hydrophilic surface area of the peptide that is exposed to water. The selection of hydrophobic residues consists of residues in the transmembrane domain (residues Leu^{10} to Val^{28}) and residue names Ala, Leu, Val, Ile, Pro, Phe, Met and Trp. Hydrophilic residues chosen were the non-hydrophobic residues in the transmembrane range.

PDB and BMRB accession codes: The atomic coordinates of Ost4 and Ost4V23D have been deposited in the Protein Data Bank (PDB) and the BioMangetic Resonance Bank (BMRB) with the accession numbers 6XCR and 6XCU for the PDB and 30760 and 30761 for the BMRB, respectively.

Funding: This research was supported by the National Science Foundation (CHE-1807722 and DBI-1726397 to SM). A portion of this work was performed at the National High Magnetic Field Laboratory, Tallahassee, FL, which is supported by NSF Cooperative Agreement No. DMR-1644779 and the State of Florida.

Acknowledgements: We thank Dr. Chengdong Huang for collecting some of the NMR data associated with this project. We thank Dr. Donghua Zhou of Oklahoma State University, OK for many useful discussions and Dr. Thomas Webb of Auburn University, Auburn, AL and Mr. Amit Kumar for the critical reading of the manuscript.

Abbreviations: OST, Oligosaccharyltransferase; DolPP, dolichol pyrophosphate; ER, Endoplasmic Reticulum; DPC, Dodecylphosphocholine; CSP, Chemical Shift Perturbation; CD, Circular Dichroism, NMR, Nuclear Magnetic Resonance, MD, Molecular Dynamics; SASA, Solvent Accessible Surface Area; PME, Particle Mesh Ewald; DPPC, dipalmitoylphosphatidylcholine

Author Contributions: S. M conceived the idea, designed the strategies and techniques employed, supervised the research, and analyzed the data. B. C performed protein expression and purification, NMR data collection, processing, NMR assignments, structure calculation, and MD simulation. D. Z contributed to NMR assignments and structure calculation. M. M performed MD simulation of the membrane-bound OST complex, SASA calculation, and analysis. All authors contributed to manuscript writing.

Competing interest: Authors declare no conflict of interest.

References:

Bai L, Wang T, Zhao G, Kovach A, Li H. 2018. The atomic structure of a eukaryotic oligosaccharyltransferase complex. *Nature* 555: 328-33

Berendsen HJC, van der Spoel D, van Drunen R. 1995. GROMACS: A message-passing parallel molecular dynamics implementation. *Computer Physics Communications* 91: 43-56

Breitling J, Aebi M. 2013. N-linked protein glycosylation in the endoplasmic reticulum. *Cold Spring Harb Perspect Biol* 5: a013359

Brunger AT, Adams PD, Clore GM, DeLano WL, Gros P, et al. 1998. Crystallography & NMR system: A new software suite for macromolecular structure determination. *Acta Crystallogr D Biol Crystallogr* 54: 905-21

Case D, Ben-Shalom I, Brozell S, Cerutti D, Cheatham III T, et al. AMBER 2018; 2018. *University of California, San Francisco*

Chaudhary B, Mazumder S, Mohanty S. 2017. Production and biophysical characterization of a mini-membrane protein, Ost4V23D: A functionally important mutant of yeast oligosaccharyltransferase subunit Ost4p. *Protein Expr Purif* 139: 43-48

Chaudhary BP, Zoetewey D, Mohanty S. 2020. (1)H, (13)C, (15)N resonance assignments and secondary structure of yeast oligosaccharyltransferase subunit Ost4 and its functionally important mutant Ost4V23D. *Biomol NMR Assign*

Chavan M, Lennarz W. 2006. The molecular basis of coupling of translocation and N-glycosylation. *Trends Biochem Sci* 31: 17-20

Cherepanova N, Shrimal S, Gilmore R. 2016. N-linked glycosylation and homeostasis of the endoplasmic reticulum. *Curr Opin Cell Biol* 41: 57-65

Delaglio F, Grzesiek S, Vuister GW, Zhu G, Pfeifer J, Bax A. 1995. NMRPipe: a multidimensional spectral processing system based on UNIX pipes. *J Biomol NMR* 6: 277-93

Dempski RE, Jr., Imperiali B. 2002. Oligosaccharyl transferase: gatekeeper to the secretory pathway. *Curr Opin Chem Biol* 6: 844-50

Dmitriev O, Jones PC, Jiang W, Fillingame RH. 1999. Structure of the membrane domain of subunit b of the Escherichia coli F0F1 ATP synthase. *J Biol Chem* 274: 15598-604

Essmann U, Perera L, Berkowitz ML, Darden T, Lee H, Pedersen LG. 1995. A smooth particle mesh Ewald method. *The Journal of Chemical Physics* 103: 8577-93

Fernandez C, Hilty C, Wider G, Wuthrich K. 2002. Lipid-protein interactions in DHPC micelles containing the integral membrane protein OmpX investigated by NMR spectroscopy. *Proc Natl Acad Sci U S A* 99: 13533-7

Freeze HH. 2013. Understanding human glycosylation disorders: biochemistry leads the charge. *J Biol Chem* 288: 6936-45

Gahmberg CG, Tolvanen M. 1996. Why mammalian cell surface proteins are glycoproteins. *Trends Biochem Sci* 21: 308-11

Gayen S, Kang C. 2011. Solution structure of a human minimembrane protein Ost4, a subunit of the oligosaccharyltransferase complex. *Biochem Biophys Res Commun*

409: 572-6
Girvin ME, Rastogi VK, Abildgaard F, Markley JL, Fillingame RH. 1998. Solution structure of the transmembrane H+-transporting subunit c of the F1F0 ATP synthase. *Biochemistry* 37: 8817-24
Grigorian A, Mkhikian H, Demetriou M. 2012. Interleukin-2, Interleukin-7, T cell-mediated autoimmunity, and N-glycosylation. *Ann N Y Acad Sci* 1253: 49-57
Grzesiek S, Bax A. 1992. Correlating backbone amide and side chain resonances in larger proteins by multiple relayed triple resonance NMR. *Journal of the American Chemical Society* 114: 6291-93
Guntert P, Buchner L. 2015. Combined automated NOE assignment and structure calculation with CYANA. *J Biomol NMR* 62: 453-71
Hansson T, Oostenbrink C, van Gunsteren W. 2002. Molecular dynamics simulations. *Current Opinion in Structural Biology* 12: 190-96
Hedger G, Rouse SL, Domański J, Chavent M, Koldsø H, Sansom MSP. 2016. Lipid-Loving ANTs: Molecular Simulations of Cardiolipin Interactions and the Organization of the Adenine Nucleotide Translocase in Model Mitochondrial Membranes. *Biochemistry* 55: 6238-49
Helenius A, Aebi M. 2004. Roles of N-linked glycans in the endoplasmic reticulum. *Annu Rev Biochem* 73: 1019-49
Hennet T, Cabalzar J. 2015. Congenital disorders of glycosylation: a concise chart of glycocalyx dysfunction. *Trends Biochem Sci* 40: 377-84
Hess B, Bekker H, Berendsen HJC, Fraaije JGEM. 1997. LINCS: A linear constraint solver for molecular simulations. *Journal of Computational Chemistry* 18: 1463-72
Hoover WG. 1985. Canonical dynamics: Equilibrium phase-space distributions. *Phys Rev A Gen Phys* 31: 1695-97
Huang C, Bhaskaran R, Mohanty S. 2012. Eukaryotic N-glycosylation occurs via the membrane-anchored C-terminal domain of the Stt3p subunit of oligosaccharyltransferase. *J Biol Chem* 287: 32450-8
Huang J, MacKerell AD, Jr. 2013. CHARMM36 all-atom additive protein force field: validation based on comparison to NMR data. *J Comput Chem* 34: 2135-45
Humphrey W, Dalke A, Schulten K. 1996. VMD: visual molecular dynamics. *J Mol Graph* 14: 33-8, 27-8
Jo S, Kim T, Iyer VG, Im W. 2008. CHARMM-GUI: A web-based graphical user interface for CHARMM. *Journal of Computational Chemistry* 29: 1859-65
Jorgensen WL, Chandrasekhar J, Madura JD, Impey RW, Klein ML. 1983. Comparison of simple potential functions for simulating liquid water. *The Journal of Chemical Physics* 79: 926-35
Kang C, Li Q. 2011. Solution NMR study of integral membrane proteins. *Current opinion in chemical biology* 15: 560-69
Karaoglu D, Kelleher DJ, Gilmore R. 1997. The highly conserved Stt3 protein is a subunit of the yeast oligosaccharyltransferase and forms a subcomplex with Ost3p and Ost4p. *J Biol Chem* 272: 32513-20
Kay L, Keifer P, Saarinen T. 1992. Pure absorption gradient enhanced heteronuclear single quantum correlation spectroscopy with improved sensitivity. *Journal of the American Chemical Society* 114: 10663-65
Kelleher DJ, Gilmore R. 2006. An evolving view of the eukaryotic

oligosaccharyltransferase. *Glycobiology* 16: 47R-62R
Kim H, Park H, Montalvo L, Lennarz WJ. 2000. Studies on the role of the hydrophobic domain of Ost4p in interactions with other subunits of yeast oligosaccharyl transferase. *Proc Natl Acad Sci U S A* 97: 1516-20
Kim H, Yan Q, Von Heijne G, Caputo GA, Lennarz WJ. 2003. Determination of the membrane topology of Ost4p and its subunit interactions in the oligosaccharyltransferase complex in Saccharomyces cerevisiae. *Proc Natl Acad Sci U S A* 100: 7460-4
Koradi R, Billeter M, Wüthrich K. 1996. MOLMOL: A program for display and analysis of macromolecular structures. *Journal of Molecular Graphics* 14: 51-55
Kornfeld R, Kornfeld S. 1985. Assembly of asparagine-linked oligosaccharides. *Annu Rev Biochem* 54: 631-64
Kumar A, Ward P, Katre UV, Mohanty S. 2012. A novel and simple method of production and biophysical characterization of a mini-membrane protein, Ost4p: a subunit of yeast oligosaccharyl transferase. *Biopolymers* 97: 499-507
Kurauskas V, Hessel A, Ma P, Lunetti P, Weinhäupl K, et al. 2018. How Detergent Impacts Membrane Proteins: Atomic-Level Views of Mitochondrial Carriers in Dodecylphosphocholine. *The Journal of Physical Chemistry Letters* 9: 933-38
Larkin A, Imperiali B. 2011. The expanding horizons of asparagine-linked glycosylation. *Biochemistry* 50: 4411-26
Laskowski RA, Rullmannn JA, MacArthur MW, Kaptein R, Thornton JM. 1996. AQUA and PROCHECK-NMR: programs for checking the quality of protein structures solved by NMR. *J Biomol NMR* 8: 477-86
Lee J, Cheng X, Swails JM, Yeom MS, Eastman PK, et al. 2016. CHARMM-GUI Input Generator for NAMD, GROMACS, AMBER, OpenMM, and CHARMM/OpenMM Simulations Using the CHARMM36 Additive Force Field. *Journal of Chemical Theory and Computation* 12: 405-13
Lee W, Tonelli M, Markley JL. 2015. NMRFAM-SPARKY: enhanced software for biomolecular NMR spectroscopy. *Bioinformatics* 31: 1325-7
Li H, Chavan M, Schindelin H, Lennarz WJ, Li H. 2008. Structure of the oligosaccharyl transferase complex at 12 A resolution. *Structure* 16: 432-40
Lim LZ, Ee S, Fu J, Tan Y, He CY, Song J. 2017. Kinetoplastid membrane protein-11 adopts a four-helix bundle fold in DPC micelle. *FEBS Lett* 591: 3793-804
Lizak C, Gerber S, Numao S, Aebi M, Locher KP. 2011. X-ray structure of a bacterial oligosaccharyltransferase. *Nature* 474: 350-55
Mashaghi A, Partovi-Azar P, Jadidi T, Nafari N, Maass P, et al. 2012. Hydration strongly affects the molecular and electronic structure of membrane phospholipids. *The Journal of Chemical Physics* 136: 114709
Matsumoto S, Shimada A, Nyirenda J, Igura M, Kawano Y, Kohda D. 2013. Crystal structures of an archaeal oligosaccharyltransferase provide insights into the catalytic cycle of N-linked protein glycosylation. *Proc Natl Acad Sci U S A* 110: 17868-73
Mohanty S, Chaudhary BP, Zoetewey D. 2020. Structural Insight into the Mechanism of N-Linked Glycosylation by Oligosaccharyltransferase. *Biomolecules* 10
Mohorko E, Glockshuber R, Aebi M. 2011. Oligosaccharyltransferase: the central enzyme of N-linked protein glycosylation. *J Inherit Metab Dis* 34: 869-78

Mueller S, Wahlander A, Selevsek N, Otto C, Ngwa EM, et al. 2015. Protein degradation corrects for imbalanced subunit stoichiometry in OST complex assembly. *Mol Biol Cell* 26: 2596-608

Muhandiram DR, Kay LE. 1994. Gradient-Enhanced Triple-Resonance Three-Dimensional NMR Experiments with Improved Sensitivity. *Journal of Magnetic Resonance, Series B* 103: 203-16

Neumoin A, Arshava B, Becker J, Zerbe O, Naider F. 2007. NMR studies in dodecylphosphocholine of a fragment containing the seventh transmembrane helix of a G-protein-coupled receptor from Saccharomyces cerevisiae. *Biophys J* 93: 467-82

Norwood TJ, Boyd,J.,Heritage,J.E.,Soffe,N.,andCampbell, I. D. 1990. Comparison of techniques for 1H-detected heteronuclear 1H-15N Spectroscopy. *J. Magn. Reson.* 87: 488-501

Nosé S, Klein ML. 1983. Constant pressure molecular dynamics for molecular systems. *Molecular Physics* 50: 1055-76

Parrinello M, Rahman A. 1981. Polymorphic transitions in single crystals: A new molecular dynamics method. *Journal of Applied Physics* 52: 7182-90

Pettersen EF, Goddard TD, Huang CC, Couch GS, Greenblatt DM, et al. 2004. UCSF Chimera--a visualization system for exploratory research and analysis. *J Comput Chem* 25: 1605-12

Ramirez AS, Kowal J, Locher KP. 2019. Cryo-electron microscopy structures of human oligosaccharyltransferase complexes OST-A and OST-B. *Science* 366: 1372-75

Rastogi VK, Girvin ME. 1999. Structural changes linked to proton translocation by subunit c of the ATP synthase. *Nature* 402: 263-8

Renault M, Saurel O, Demange P, Reat V, Milon A. 2010. Solution-State NMR Spectroscopy of Membrane Proteins in Detergent Micelles: Structure of the Klebsiella pneumoniae Outer Membrane Protein A, KpOmpA In *Membrane Protein Structure Determination: Methods and Protocols*, ed. J-J Lacapère, pp. 321-39. Totowa, NJ: Humana Press

Schrodinger L. 2015. The Pymol Molecular Graphics System, Version~1.8.

Schulz BL, Stirnimann CU, Grimshaw JP, Brozzo MS, Fritsch F, et al. 2009. Oxidoreductase activity of oligosaccharyltransferase subunits Ost3p and Ost6p defines site-specific glycosylation efficiency. *Proc Natl Acad Sci U S A* 106: 11061-6

Shen Y, Delaglio F, Cornilescu G, Bax A. 2009. TALOS+: a hybrid method for predicting protein backbone torsion angles from NMR chemical shifts. *J Biomol NMR* 44: 213-23

Shrimal S, Gilmore R. 2018. Oligosaccharyltransferase structures provide novel insight into the mechanism of asparagine-linked glycosylation in prokaryotic and eukaryotic cells. *Glycobiology*

Spirig U, Bodmer D, Wacker M, Burda P, Aebi M. 2005. The 3.4-kDa Ost4 protein is required for the assembly of two distinct oligosaccharyltransferase complexes in yeast. *Glycobiology* 15: 1396-406

Szymanski CM, Wren BW. 2005. Protein glycosylation in bacterial mucosal pathogens. *Nat Rev Microbiol* 3: 225-37

Szyperski T, Vandenbussche G, Curstedt T, Ruysschaert JM, Wuthrich K, Johansson J.

1998. Pulmonary surfactant-associated polypeptide C in a mixed organic solvent transforms from a monomeric alpha-helical state into insoluble beta-sheet aggregates. *Protein Sci* 7: 2533-40

Tieleman DP, van der Spoel D, Berendsen HJC. 2000. Molecular Dynamics Simulations of Dodecylphosphocholine Micelles at Three Different Aggregate Sizes: Micellar Structure and Chain Relaxation. *The Journal of Physical Chemistry B* 104: 6380-88

Wacker M, Linton D, Hitchen PG, Nita-Lazar M, Haslam SM, et al. 2002. N-linked glycosylation in Campylobacter jejuni and its functional transfer into E. coli. *Science* 298: 1790-3

Wang Y, Tajkhorshid E. 2008. Electrostatic funneling of substrate in mitochondrial inner membrane carriers. *Proc Natl Acad Sci U S A* 105: 9598-603

Wild R, Kowal J, Eyring J, Ngwa EM, Aebi M, Locher KP. 2018. Structure of the yeast oligosaccharyltransferase complex gives insight into eukaryotic N-glycosylation. *Science* 359: 545-50

Yan A, Lennarz WJ. 2005. Two oligosaccharyl transferase complexes exist in yeast and associate with two different translocons. *Glycobiology* 15: 1407-15

Zhang O, Kay LE, Olivier JP, Forman-Kay JD. 1994. Backbone 1H and 15N resonance assignments of the N-terminal SH3 domain of drk in folded and unfolded states using enhanced-sensitivity pulsed field gradient NMR techniques. *Journal of Biomolecular NMR* 4: 845-58

Zubkov S, Lennarz WJ, Mohanty S. 2004. Structural basis for the function of a minimembrane protein subunit of yeast oligosaccharyltransferase. *Proc Natl Acad Sci U S A* 101: 3821-6

Tables

Table I. Structural statistics of the solution NMR structure of Ost4 and Ost4V23D

Distance restraints	Ost4	Ost4V23D
Unambiguous	189	195
Intra residue, |i-j|=0	54	46
Sequential, |i-j|<=1	73	74
Medium range, 1<|i-j|<5	62	75
Long range, |i-j|>=5	0	0
Hydrogen bond restraints	27	27
Dihedral angle restraints	68	62
Interresidue distance restraints violations		
Violations	0	0
RMSD to average structures, Å		
Backbone (residues 4-32)	0.24	0.20
Heavy atoms (residues 4-32)	0.89	0.90
Ramachandran plot outliers, %		
Residues in most favored regions	97.1 %	91.4%
Residues in additionally allowed regions	2.9 %	8.6 %
Residues in generously allowed regions	0.0 %	0%
Residues in disallowed regions	0.0 %	0%

Table II. Average minimum distance between atoms of Ost4 residue 23 and partner residues from molecular dynamics trajectories of WT and V23D mutant. Values are reported in Angstroms with standard error of the mean reported in parentheses. These average and standard errors were computed over the last 500 ns of simulation

Partner Residue	WT (Å)	V23D (Å)	V23D-WT (Å)
Stt3L145	4.716(3)	5.797(3)	1.081(4)
Stt3F425	3.082(2)	5.172(4)	2.090(4)
Stt3L429	2.483(2)	3.959(4)	1.476(5)
Stt3K448	9.152(3)	2.174(3)	-6.978(4)
Stt3I456	2.276(1)	2.484(2)	0.207(2)
Stt3L459	3.151(3)	5.363(4)	2.211(5)

Figure Legends:

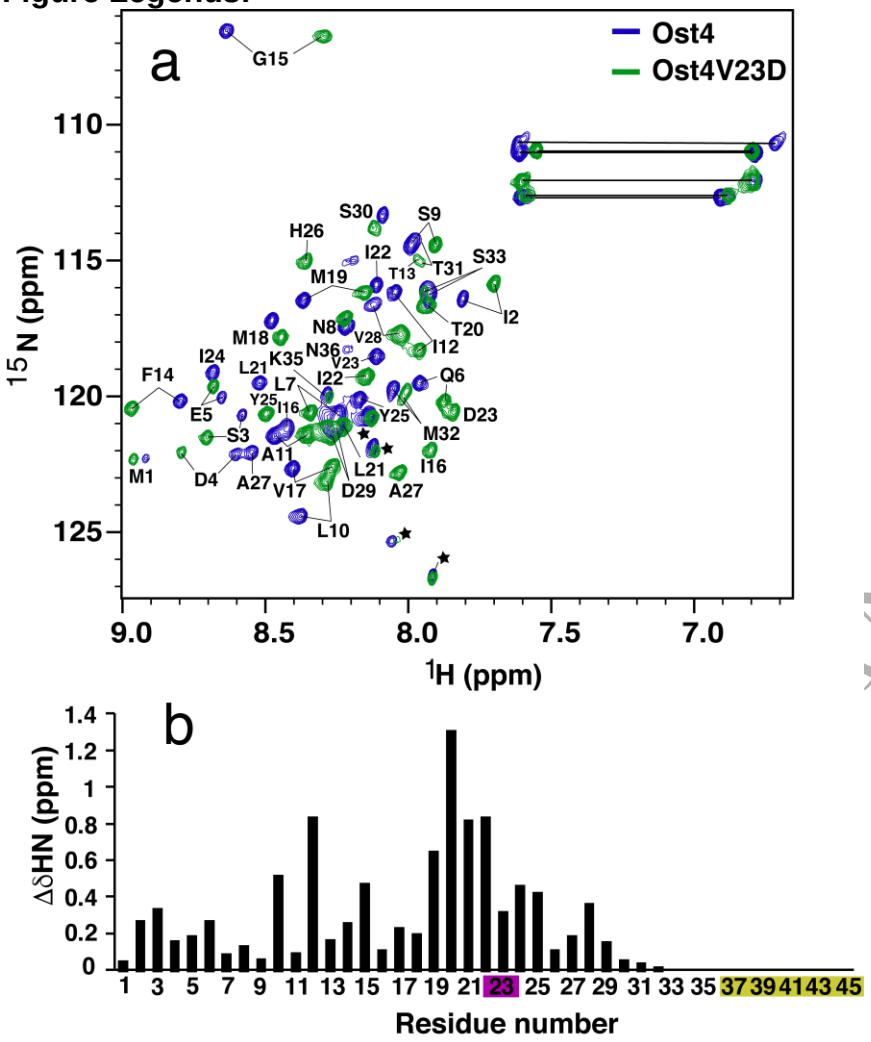

Fig. 1: (a) Overlay of 2D {^{1}H, ^{15}N} HSQC of Ost4 (blue) with Ost4V23D (green). The C-terminal tag residues that do not belong to Ost4 or Ost4V23D protein are indicated by * in the spectrum. (b) The plot of the chemical shift perturbations (CSP) upon mutation of valine at position 23 to aspartate. The resonances close to the mutation site for residues L21, I22, D23, and A27are perturbed significantly showing CSP >0.5 ppm. Residue number 1- 36 belong to Ost4 and Ost4V23D. The mutated residue D23 is highlighted in purple. The C-terminal tag residues 37 to 45 (highlighted in yellow) do not belong to Ost4 or Ost4V23D.

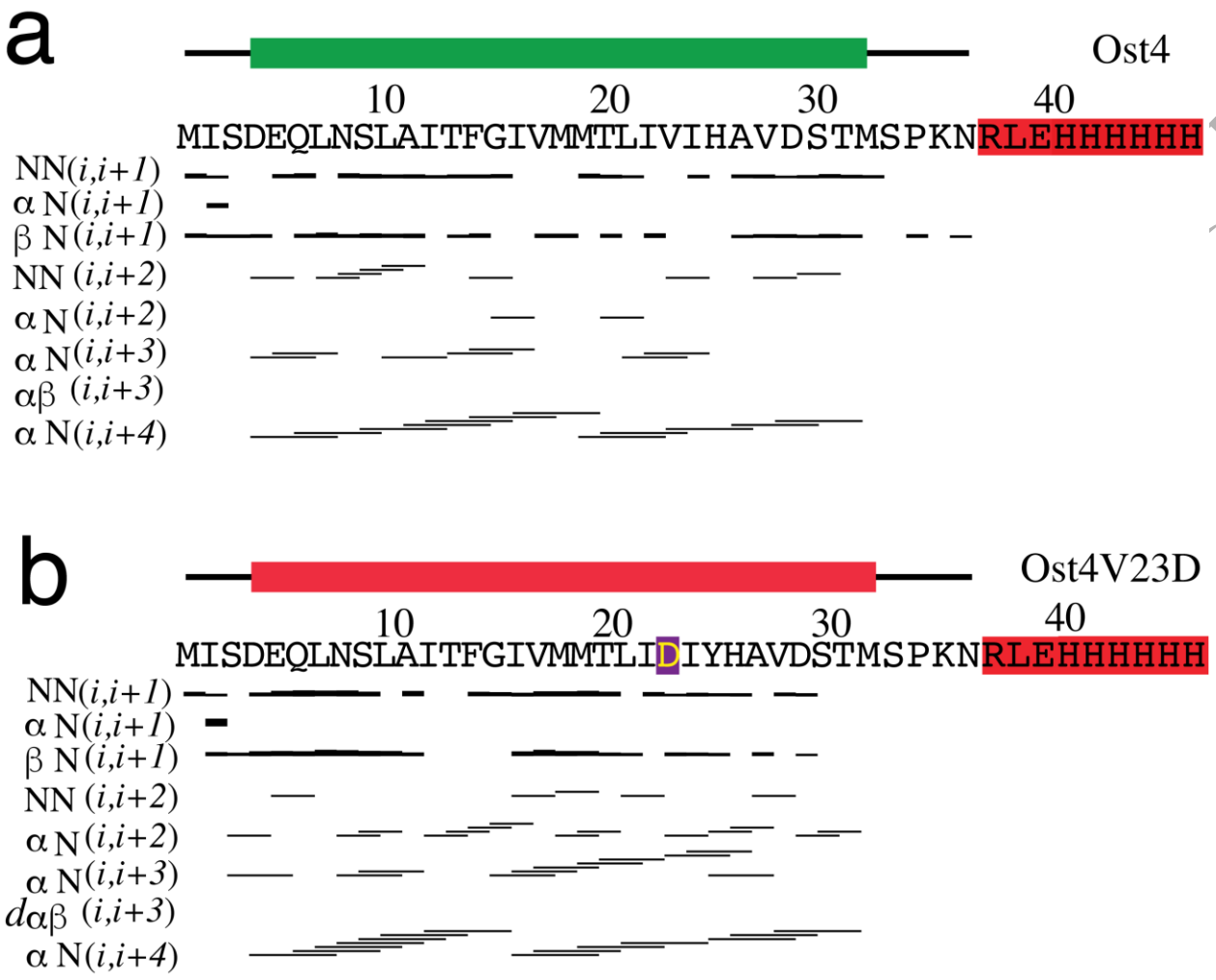

Fig. 2: Predicted secondary structure, sequence, and summary of sequential NOE contacts of Ost4 (a) and Ost4V23D (b). The secondary structural elements were based on the secondary chemical shift ⊗™^{13}C⟨, ⊗™^{13}C⟨-⊗™^{13}C®, and TALOS+ (Chaudhary et al 2020). The residue in yellow highlighted in purple is the mutated residue in Ost4V23D. The C-terminal tag residues (highlighted in red) do not belong to Ost4 or Ost4V23D.

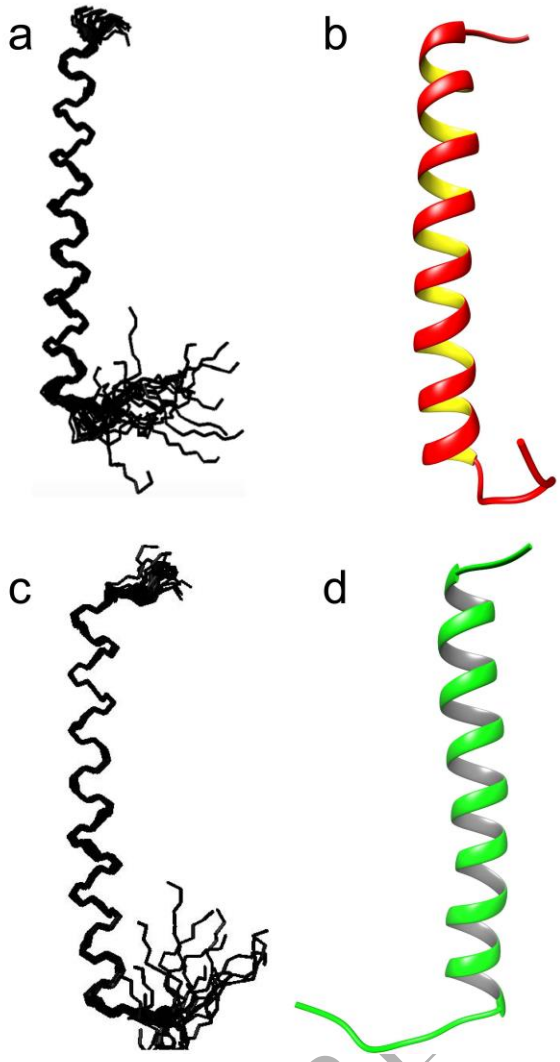

Fig. 3: The ensembles of the 20 lowest-energy NMR structures of (a) Ost4 and (c) Ost4V23D after solvent refinement. Ribbon drawing of one of the 20 energy-minimized conformers: wild type Ost4 (b), and Ost4V23D mutant (d). Both proteins exist as ⟨-helices in dodecylphosphocholine (DPC) micelles in phosphate buffer at pH 6.5.

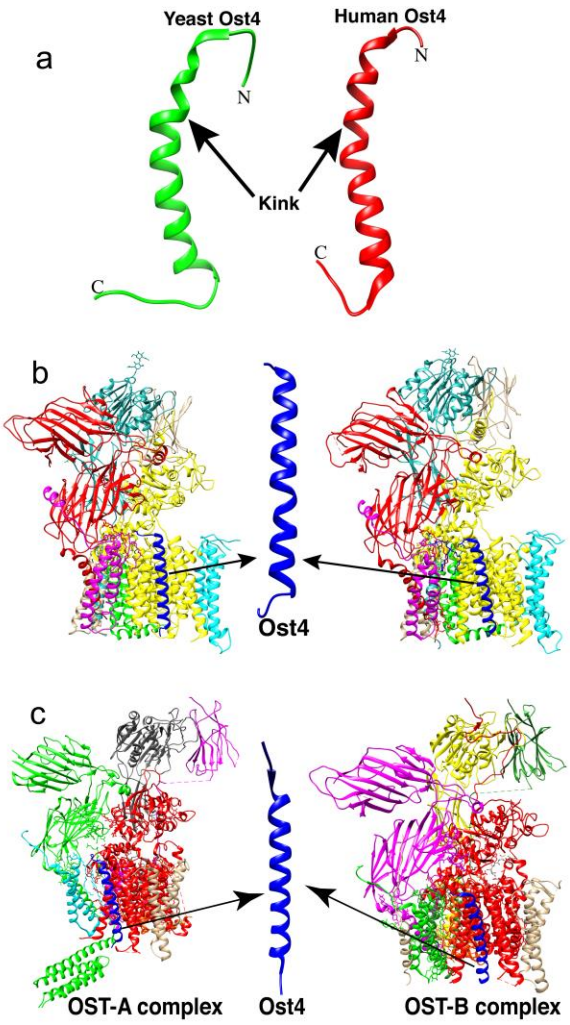

Fig. 4: (a) NMR structures of chemically synthesized yeast Ost4 (PDB ID 1rkl) and human Ost4 (PDB ID 2lat) in mixed organic solvents. Both the structures contain a kinked helix. (b) Cryo-EM structures of yeast OST complex in nanodisc (PDB ID 6ezn) or digitonin (PDB ID 6c26). Ost4 is shown as a single straight helix in blue. (c) Cryo-EM structures of human OST-A (PDB ID 6s7o) and OST-B (PDB ID 6s7t) showing Ost4 subunit as a single straight helix in blue. The structures were generated by Chimera.

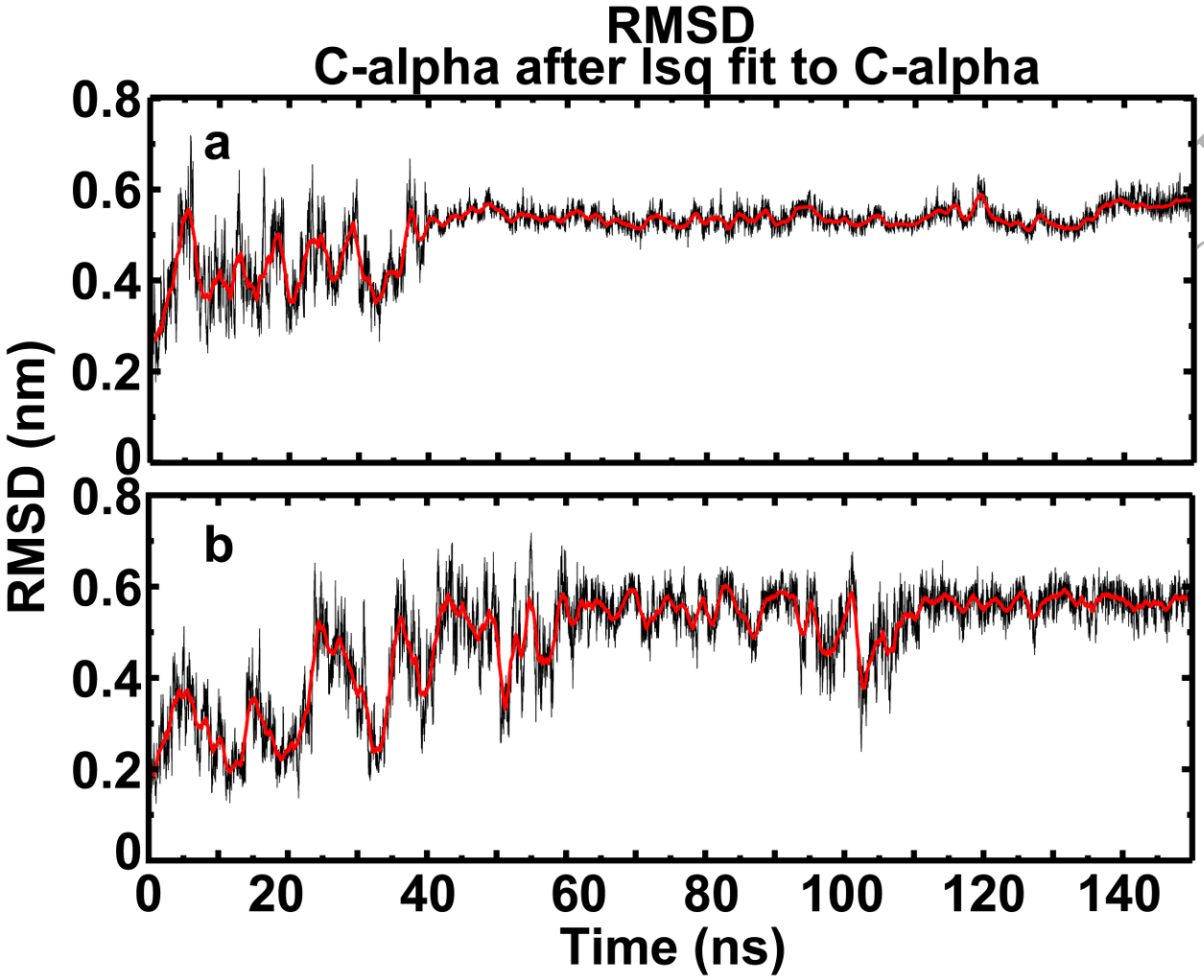

Fig. 5: Root mean squared deviation (RMSD) of C〈 of Ost4 (A) and Ost4V23D (B). Each simulation reached a stable RMSD of ~0.6 nm during the 150 ns molecular dynamics run. For each MD simulation, the protein was inserted into a micelle containing 65 molecules of DPC.

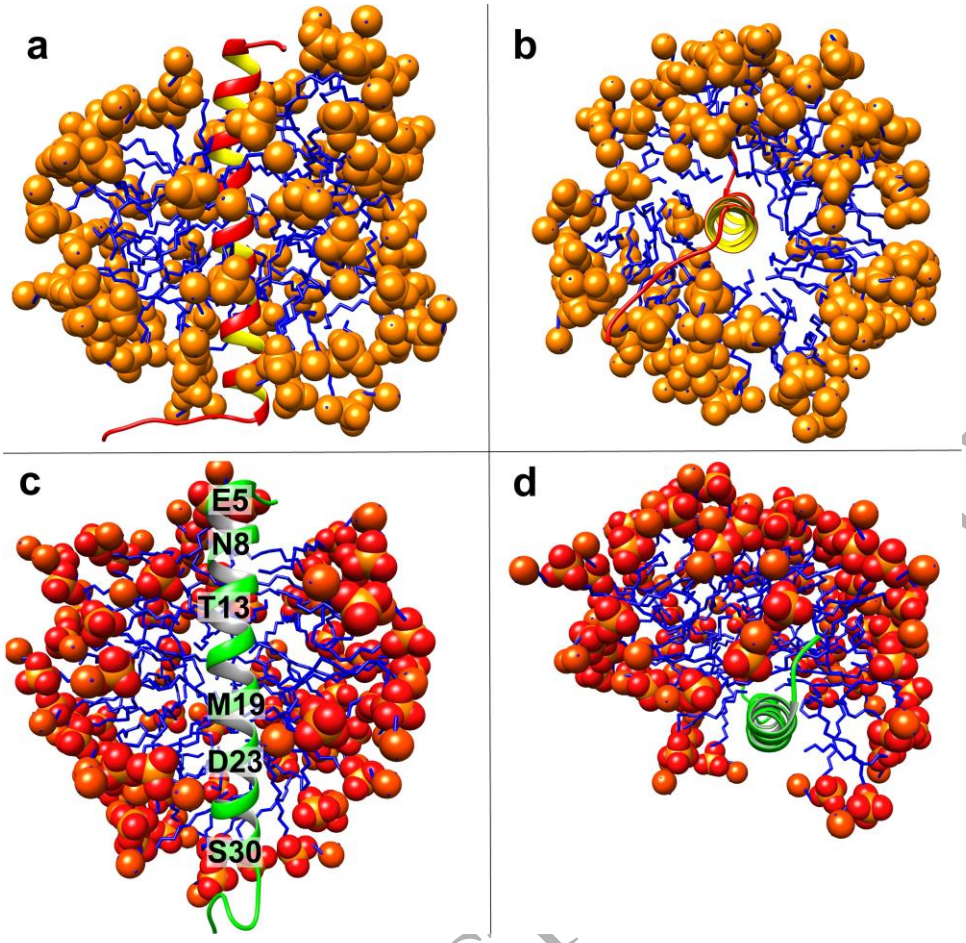

Fig. 6: Structure and orientation of Ost4 and Ost4V23D in DPC micelles at equilibrium after MD simulation: (a) side view and (b) top view of Ost4, (c) side view and (d) top view of Ost4V23D. Solvent exposed residues are labeled in panel c.

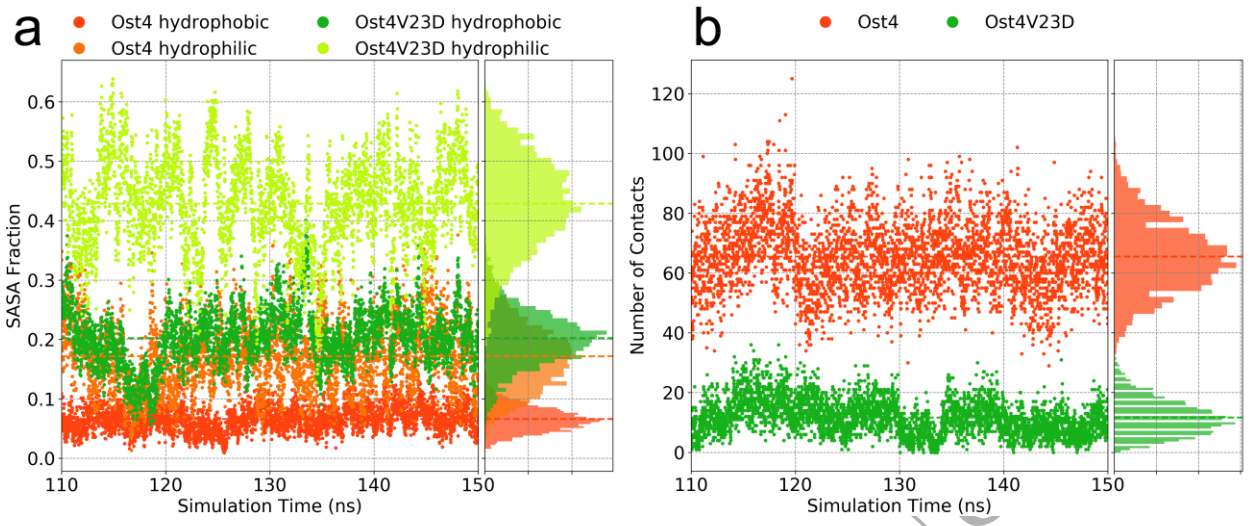

Fig. 7: Solvent and lipid exposure of Ost4 and Ost4V23D from all-atom molecular dynamics simulations. (a) Hydrophilic and hydrophobic solvent accessible surface area (SASA) of Ost4 and Ost4V23D. (b) Number of DPC-tails that make contacts with residues 10-28 of Ost4 and Ost4V23D.

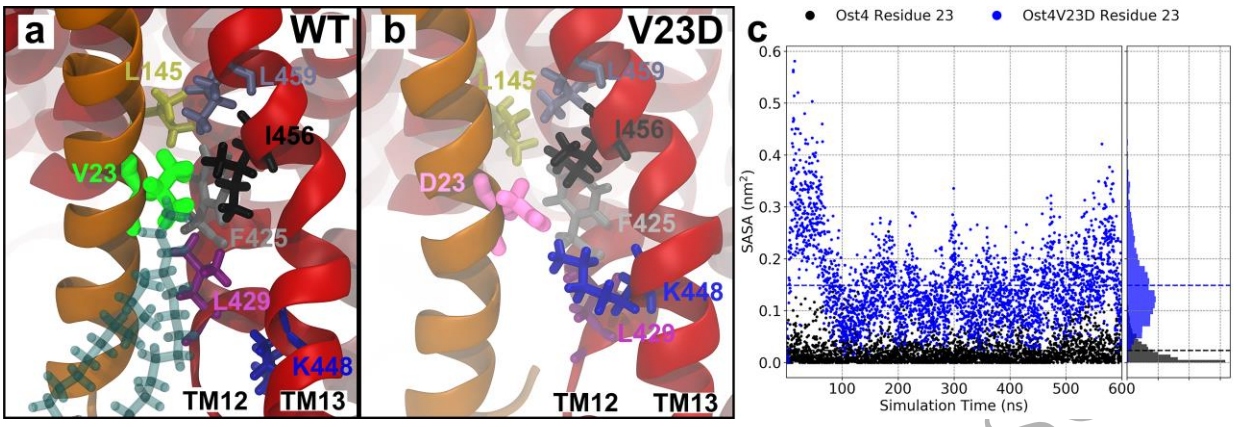

Fig. 8: Molecular dynamics simulations of the OST complex in a dipalmitoylphosphatidylcholine (DPPC) membrane. (a) A representative snapshot of the WT simulation with highlighted Ost4V23 (brown) residue and associated hydrophobic contacts from Stt3 TM 12 and 13 (red), and lipid molecules (cyan). Important residues for WT, V23D, and their interacting partners in Stt3 TM12 and 13 are labeled. (b) Representative snapshot from Ost4V23D simulation with Ost4D23-Stt3K448 salt-bridge highlighted. (c) SASA of residue 23 from 600 ns of simulation for both WT and mutant simulation.